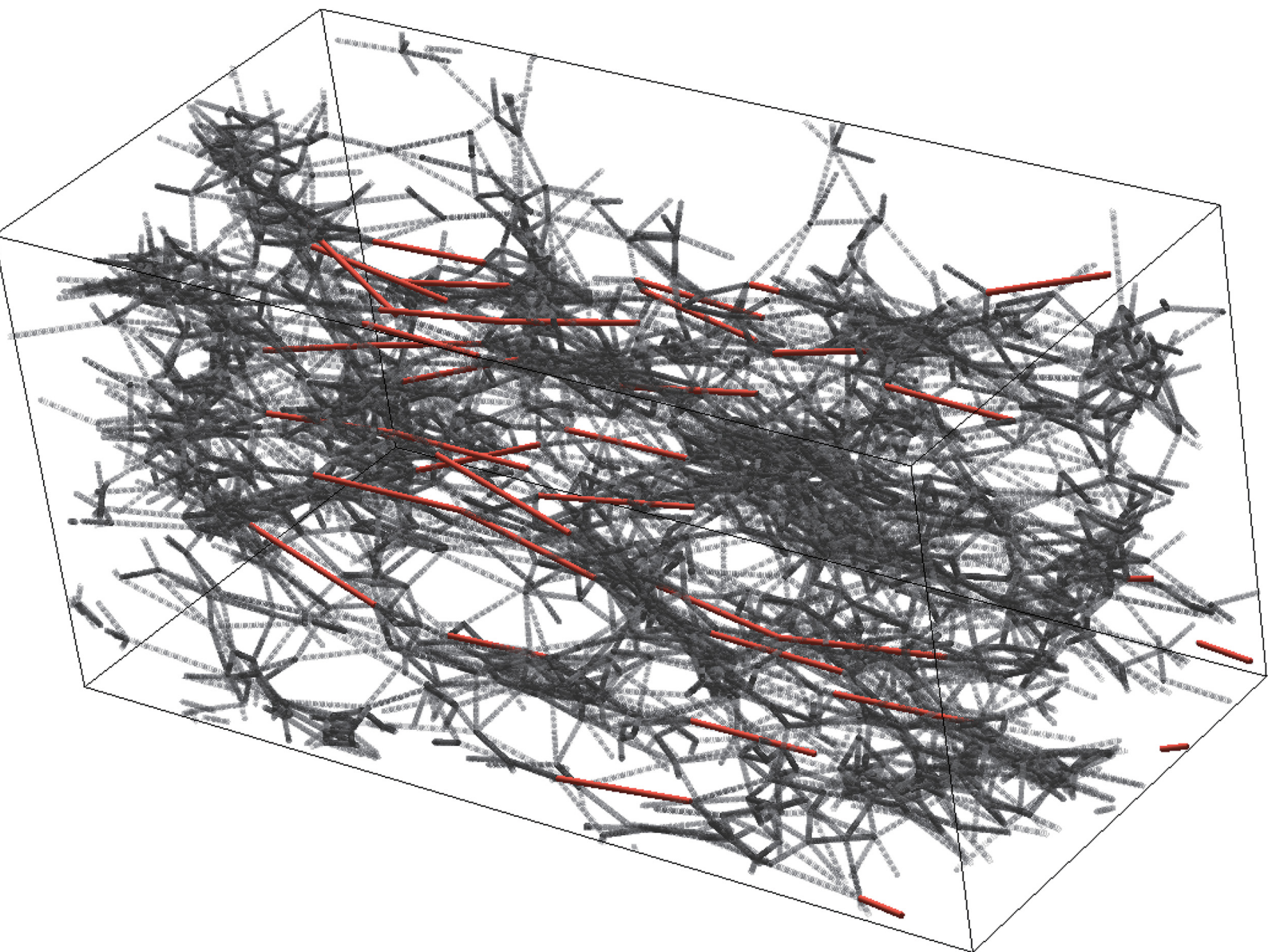


# Soft Matter

[rsc.li/soft-matter-journal](https://rsc.li/soft-matter-journal)



ISSN 1744-6848

**PAPER**

Yuichi Masubuchi *et al.*  
Phantom chain simulations for the fracture of star polymer  
networks with various strand densities



Cite this: *Soft Matter*, 2024, 20, 7103

## Phantom chain simulations for the fracture of star polymer networks with various strand densities

Yuichi Masubuchi, \* Takato Ishida, Yusuke Koide and Takashi Uneyama

Despite many attempts, the relationship between the fracture and structure of polymer networks is yet to be clarified. For this problem, a recent study on phantom chain simulations [Y. Masubuchi *et al.*, *Macromolecules*, 2023, **56**, 9359–9367.] has demonstrated that the fracture characteristics obtained for polymer networks with various node functionalities and conversion ratios lie on master curves if they are plotted against cycle rank, which is the number of closed loops in the network per network node. In this study, we extended the simulation to the effect of prepolymer concentration  $c$  on the relationships between the cycle rank and fracture characteristics within the concentration range of  $1 \lesssim c/c^* \lesssim 10$ , concerning the overlapping concentration  $c^*$ . We created networks from sols of star-branched phantom bead-spring chains *via* an end-linking reaction between different chains through Brownian dynamics simulations upon varying the number of branching arms  $f$  from 1 to 8, and the conversion ratio  $\varphi_c$  from 0.6 to 0.95. For the resultant networks, the cycle rank  $\xi$  was consistent with the mean-field theory. The networks were uniaxially stretched with energy minimization until break to obtain modulus  $G$ , strain at break  $\varepsilon_b$ , stress at break  $\sigma_b$ , and work for fracture  $W_b$ . As reported earlier,  $\varepsilon_b$  data for various  $f$  and  $\varphi_c$  are located on a master curve if plotted against  $\xi$ . The other quantities also draw master curves as functions of  $\xi$  if normalized by the branch point density  $\nu_{br}$ . The master curves depend on  $c$ ; as  $c$  increases, all the mechanical characteristics monotonically increase. If we plot  $\sigma_b/\nu_{br}$  and  $W_b/\nu_{br}$  against  $G/\nu_{br}$ , the data for various  $f$  and  $\varphi_c$  lie on master curves but depending on  $c$ . Consequently, the fracture characteristics are not solely described by the modulus.

Received 14th June 2024,  
Accepted 14th August 2024

DOI: 10.1039/d4sm00726c

[rsc.li/soft-matter-journal](http://rsc.li/soft-matter-journal)

### Introduction

Much clarification is needed on which structural characteristics dominate the fracture of polymer networks.<sup>1</sup> A few theoretical attempts have been reported focusing on the effect of loops and crack propagation. Barney *et al.*<sup>2</sup> extended the real elastic network theory (RENT)<sup>3</sup> to describe the fracture energy. RENT elaborately describes the effect of loops on the modulus, considering not only primary loops (trivial loops) but also higher-order loops; here, a primary loop means a linear chain with the chain ends connected to a single branch point and does not sustain stress. In contrast, secondary and higher-order loops contribute to stress because they are closed structures consisting of some branch points. Combining such a loop-dependent modulus and Lake–Thomas theory,<sup>4</sup> Barney *et al.*<sup>2</sup> proposed a theoretical expression of the work for crack propagation in tearing tests. They demonstrated that the theoretical prediction is consistent with coarse-grained molecular simulations, in which they varied the conversion ratio and the strand molecular weight. (Here, the conversion ratio means the ratio

of the reacted chain ends of prepolymers to their total number, including unreacted ones.) Lin and Zhao<sup>5</sup> reported a different theoretical attempt in which they calculated fracture energy considering crack tip propagation. According to this theory, the fracture energy increases with an increase in secondary loops (cyclic loops), contradicting Barney *et al.*<sup>2</sup> Wang *et al.*<sup>6</sup> extended Lake–Thomas theory according to the work for the opening of a loop at the crack tip considering the roles of the unbroken portion.<sup>7</sup> Their fracture energy increases with the number of prepolymers and branch points in the subjected loop.

Several experimental results have been reported that these theories cannot describe. For instance, Akagi *et al.*<sup>8</sup> observed the fracture of tetra-PEG gels created with various conversion ratios and prepolymer concentrations. Because their networks are made from mixtures of star polymers where each molecule reacts only with the other, primary and higher odd-ordered loops (*i.e.*, circles formed by an odd number of prepolymers) are excluded. Although they observed fracture under uniaxial stretch without an initial notch, the fracture energy and modulus correlate for gels with various conversion ratios, similar to Lake–Thomas theory. However, the prepolymer concentration dependence is not solely described by the modulus. The other example reported by Fujiyabu *et al.*<sup>9</sup> is that gels made from

Department of Materials Physics, Nagoya University, Nagoya 4649603, Japan.  
E-mail: [mas@mp.pse.nagoya-u.ac.jp](mailto:mas@mp.pse.nagoya-u.ac.jp)

3-arm star prepolymers exhibit better fracture properties than those made from 4-arm analogs, even if the modulus is the same. They explained this difference by stretch-induced crystallization of the 3-arm case. However, Masubuchi *et al.*<sup>10</sup> demonstrated that the superiority of 3-arm gels is seen even without crystallization using coarse-grained molecular simulations.

An interesting clue for network fracture is cycle rank. Masubuchi *et al.*<sup>11</sup> performed coarse-grained simulations for elastic networks prepared from star branch prepolymers to obtain strain and stress at break and work for fracture under uniaxial elongations. They found that for the networks with various branch functionalities (*i.e.*, the number of branching arms for star prepolymers for this specific case) and conversion ratios with monodisperse arm lengths, some fracture characteristics follow master curves if plotted against cycle rank. Masubuchi<sup>12</sup> also showed that fracture characteristics for networks created from mixtures of star polymers with different functionalities lie on the same master curves as those made from monodisperse sols. In the subsequent work, Masubuchi<sup>13</sup> further examined end-linking networks composed of linear prepolymers and multi-functional linkers to report that the relationship between the fracture characteristics and cycle rank is essentially the same as that of star polymer networks despite including primary and higher-order loops.

This study used phantom chain simulations to explore the relationship between the fracture properties and cycle rank for cases with different prepolymer concentrations. Consistent with earlier studies,<sup>1,10,14–16</sup> the simulation results showed that the modulus and work for fracture increase with an increase in the prepolymer concentration. The master curves concerning the relation between the fracture properties and cycle rank hold for various prepolymer functionalities and conversion ratios. However, they depend on the prepolymer concentration in a different manner from that of the modulus. The details are shown below.

## Model and simulations

The employed model and simulation scheme are shared with the previous studies,<sup>10–13,17</sup> except for the prepolymer density. Examined networks were created from equilibrated sols of phantom star chains with various concentrations through Brownian simulations with end-linking reactions. The obtained networks were energy-minimized and stretched until break. During the elongation, the evolution of stress was recorded as a function of strain, and from the stress–strain relationship thus obtained, the fracture characteristics were extracted. For technical details, see the previous work<sup>10</sup> and its SI.

The prepolymers are represented by bead-spring chains, for which  $f$ -arms are connected to the central bead. Since we only deal with end-linking reactions,  $f$  corresponds to the functionality of nodes in the resultant networks. The bead number of each arm is  $N_a$ . A sufficiently large number of prepolymers  $M$  were dispersed with several bead number densities  $\rho$  in cubic simulation boxes with periodic boundary conditions and

equilibrated *via* Brownian dynamics. The equation of motion for the position of each bead  $\mathbf{R}_i$  is written as follows.

$$\mathbf{0} = -\zeta \dot{\mathbf{R}}_i + \frac{3k_B T}{a^2} \sum_k f_{ik} \mathbf{b}_{ik} + \mathbf{F}_i \quad (1)$$

The first term on the right-hand side is the drag force, and  $\zeta$  is the friction coefficient. The second term is the elastic force generated by springs. Here,  $a$  is the average bond length,  $\mathbf{b}_{ik}$  is the bond vector defined as  $\mathbf{b}_{ik} \equiv \mathbf{R}_i - \mathbf{R}_k$ , and  $f_{ik}$  is the non-linear spring constant written as  $f_{ik} = (1 - \mathbf{b}_{ik}^2/b_{\max}^2)^{-1}$  with the maximum stretch  $b_{\max}$ . This non-linear spring constant with finite extensibility avoids bond extension due to thermal fluctuations.  $k_B$  is the Boltzmann constant, and  $T$  is the temperature. The third term is Gaussian random force that obeys the fluctuation–dissipation relation with the first term. Since no inter-bead interactions are considered, chain overlapping and crossing are allowed. For the employed model, units of length, energy, and time are defined from this Brownian scheme as  $a$ ,  $k_B T$ , and  $\tau = \zeta a^2/k_B T$ . The quantities are normalized according to these units hereafter. Eqn (1) was numerically integrated by a second-order scheme<sup>18</sup> with the step size  $\Delta t$ .

After sufficient equilibration, end-linking reactions were turned on.<sup>19,20</sup> Following the experiments for tetra-PEG type gels,<sup>1,14</sup> prepolymers were binary labeled, and the reaction took place only between prepolymers having different labels. Thus, no primary and higher odd-order loops were included in the network, whereas secondary and higher even-order loops were naturally created. The reaction occurred with the reaction rate  $p$  when a pair of reactive ends came closer than the critical distance  $r_c$ . During the gelation, snapshots of the system with various conversion ratios  $\varphi_c$  were stored. Here, the conversion ratio is defined as  $\varphi_c \equiv N_{\text{re}}/(Mf)$  with the number of reacted chain ends  $N_{\text{re}}$ .

The networks thus obtained for various combinations of  $(\rho, f, \varphi_c)$  values were uniaxially stretched under volume conservation. The stretch was performed for energy-minimized networks, as conducted in earlier studies.<sup>21–24</sup> The total energy is written below and is consistent with the non-linear spring employed in the Brownian scheme.

$$U = -\frac{3k_B T b_{\max}^2}{2a^2} \sum_{i,k} \ln \left( 1 - \frac{\mathbf{b}_{ik}^2}{b_{\max}^2} \right) \quad (2)$$

This energy was minimized with the Broyden–Fletcher–Goldfarb–Sanno method,<sup>25</sup> in which the beads were moved within an infinitesimal distance  $\Delta r$  without Brownian motion according to the potential gradient until the total energy converged to a specific value within a given allowance  $\Delta u$ . In the energy-minimized structure, elongated bonds were removed when the bond length exceeded a certain critical length  $b_c$ . The energy-minimization and stretch steps were alternatively repeated until the network percolation was eliminated.

The advantage of the employed energy-minimized scheme is that the results are not affected by the number of parameters, such as the elongation rate and bond-cutting criterion, as discussed previously.<sup>10</sup> The drawback is the lack of thermal

motion, and we cannot discuss the energy dissipation according to the structural relaxation.<sup>26</sup>

Since the primary purpose of this study was to discuss the effect of the prepolymer concentration, the bead number density  $\rho$  was varied to 2, 4, and 16, and the results shall be compared with those for the case of  $\rho = 8$  examined in the previous study.<sup>11</sup> The number of branching arms, *i.e.*, the node functionality, was varied in a range of  $3 \leq f \leq 8$ , and the number of beads on each arm was fixed at  $N_a = 5$ . For the case of  $f = 3$  and  $N_a = 5$ , the density corresponds to  $1 \lesssim c/c^* \lesssim 8$  with respect to the overlapping concentration  $c^*$ . Due to the  $f$ -dependence of the gyration radius, the range is  $1.3 \lesssim c/c^* \lesssim 11$  for  $f = 8$ . The number of prepolymers was fixed at  $M = 1600$ . The other parameters were the same as in the previous studies.  $\Delta t = 0.01$ ,  $b_{\max} = 2$ ,  $b_c = \sqrt{1.5}$ ,  $p = 0.1$ ,  $r_c = 0.5$ ,  $0.6 \leq \varphi_c \leq 0.95$ ,  $\Delta r = 0.01$ , and  $\Delta u = 10^{-4}$ . Eight independent simulation runs were performed for each condition, and the quantities reported below are ensemble averages unless stated.

## Results and discussion

Fig. 1(a) shows the snapshots of examined networks before and after energy minimization for  $f = 4$  at  $\varphi_c = 0.95$  with various  $\rho$  values. Since the number of prepolymers  $M$  is fixed at 1600, the simulation box size decreases with an increase in  $\rho$ . Even for the largest  $\rho$  with the smallest box case, the box dimension is large enough compared to prepolymers; the box size is *ca.*  $12.8^3$  for  $f = 4$ , whereas the average end-to-end distance is  $\sqrt{10}$ . Note that  $M = 1600$  is sufficient for fracture simulations, as demonstrated previously.<sup>10</sup> Nevertheless, the effect of the system size shall be discussed later.

Concerning the network structure, the density inhomogeneity due to kinetic arrest is observed when the polymer concentration is low, as experimentally reported earlier.<sup>27</sup> See Fig. 1(b), which shows the radial distribution functions for network nodes  $g(r)$ . As  $\rho$  decreases,  $g(r)$  increases, as seen for broken curves showing the data before energy minimization. After energy minimization, the inhomogeneity is enhanced, as indicated by solid curves. Fig. 1(c) exhibits strand length distribution,  $P(r)$ . Despite spatial inhomogeneity observed for  $g(r)$ ,  $P(r)$  before energy minimization shown by broken curves implies the Gaussian distribution of the strand length. The energy minimization shrinks such strands, and in the resultant networks, the peak position of  $P(r)$  shifts towards smaller  $r$  as  $\rho$  decreases. Note, however, that  $P(r)$  is insensitive to  $\rho$  in the long-tail region, implying that the prediction of bond breakage from this distribution is not trivial. The network structures thus obtained are similar to those reported in earlier studies.<sup>21–24</sup>

Fig. 2 shows cycle rank  $\xi$  as a function of  $\varphi_c$ . Following the earlier studies,<sup>28–30</sup>  $\xi$  is defined as the difference between the number of nodes and strands per prepolymer connected to the percolated network,  $\nu$  and  $\mu$ . Such values can be directly obtained from simulation snapshots. Meanwhile, in the mean-field theory,<sup>28–30</sup> these values are calculated from the

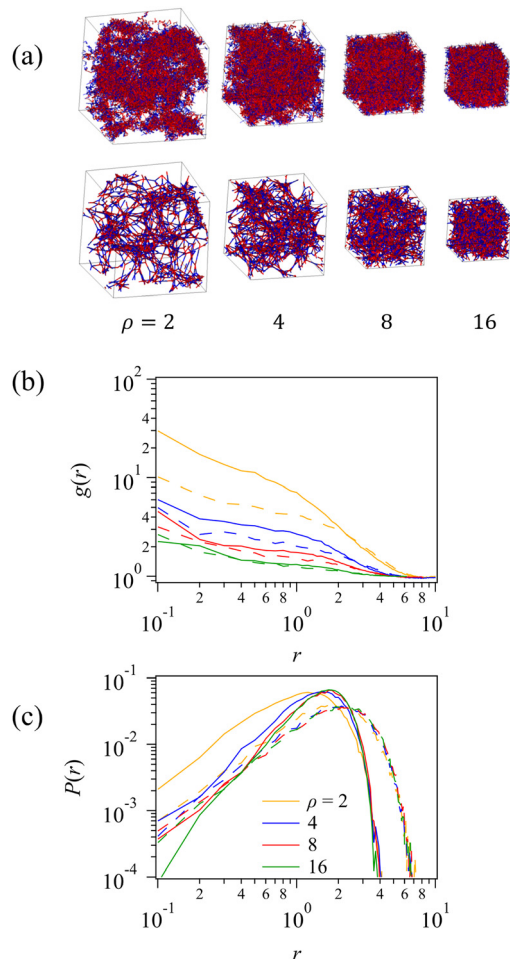


Fig. 1 Typical snapshots of examined networks after gelation (top) and after energy minimization (bottom) (a), the radial distribution of network nodes (b), and the strand length distribution (c).  $f = 4$ ,  $\varphi_c = 0.95$ , and  $\rho = 2, 4, 8$ , and 16. In panel (a), blue and red indicate different chemistries between which the end-linking reaction occurs. In panels (b) and (c), yellow, blue, red, and green curves exhibit the results for  $\rho = 2, 4, 8$ , and 16, respectively. Broken and solid curves are the results before and after energy minimization.

probability of finding an arm of the prepolymer excluded from the percolated network  $p_{\text{out}}$ , which is written as follows.

$$p_{\text{out}}(f, \varphi_c) = \varphi_c p_{\text{out}}^{f-1} + (1 - \varphi_c) \quad (3)$$

The first term on the right-hand side is the probability for the condition in which the subjected arm is reacted, and the other arms of the same polymer are excluded from the percolated network. The second term is the probability of finding the subjected arm unreacted.  $p_{\text{out}}(f, \varphi_c)$  can be numerically determined for given  $f$  and  $\varphi_c$  under the condition  $0 \leq p_{\text{out}} \leq 1$ . From  $p_{\text{out}}$ , the probability of finding a prepolymer having  $h$ -arms connected to the percolated network,  $p_{\text{eff}}(f, \varphi_c, h)$ , can be calculated as follows.

$$p_{\text{eff}}(f, \varphi_c, h) = \binom{f}{h} (1 - p_{\text{out}})^h p_{\text{out}}^{f-h} \quad (4)$$

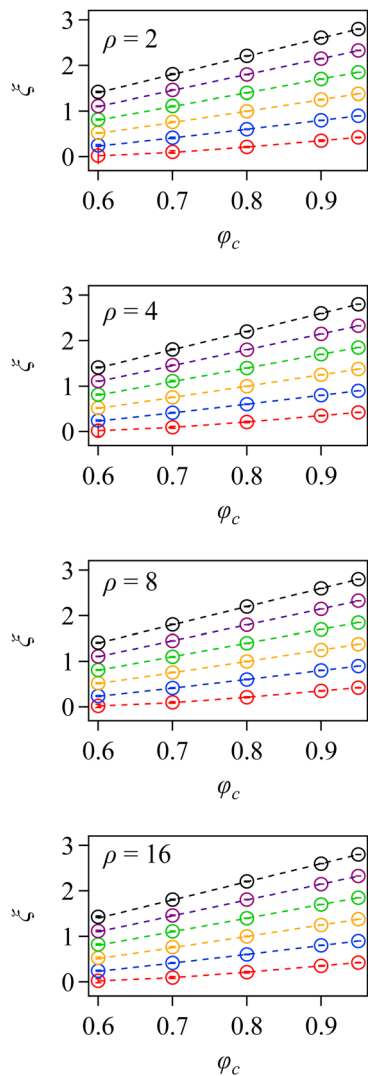


**Fig. 2** Cycle rank per branch point  $\xi$  plotted against  $\varphi_c$  for  $\rho = 2, 4, 8$ , and  $16$  from top to bottom with  $f = 3$  (red),  $4$  (blue),  $5$  (orange),  $6$  (green),  $7$  (violet), and  $8$  (black). Dotted curves indicate the mean-field calculation. Error bars (within symbols) show the standard deviation of 8 different simulation runs. Note that the results for  $\rho = 8$  were reported previously.

Here,  $\binom{f}{h}$  is the binomial coefficient. Using  $p_{\text{eff}}$ ,  $\xi$  is calculated via  $\nu$  and  $\mu$  as follows.

$$\nu(f, \varphi_s) = \sum_{h=3}^f h p_{\text{eff}}(f, \varphi_c, h) \quad (5)$$

$$\mu(f, \varphi_s) = \sum_{h=3}^f p_{\text{eff}}(f, \varphi_c, h) \quad (6)$$

$$\xi = \nu - \mu \quad (7)$$

Fig. 2 demonstrates that  $\xi$  of simulated networks (shown by symbols) does not depend on  $\rho$ , and the  $\varphi_c$ -dependence is entirely consistent with the mean-field theory,<sup>28–30</sup> as

previously reported<sup>11</sup> for the case of  $\rho = 8$ . This coincidence demonstrates that each reaction occurs independently despite structural inhomogeneity in Fig. 1. However, the correspondence of  $\xi$  among the networks with different  $\rho$  values does not mean the maturity of the effective network. Namely, inert fractions like dangling domains are not discriminated in calculating  $\xi$ , as discussed later.

Fig. 3 shows examples of the development of true stress  $\sigma$  during elongation against true strain  $\varepsilon$ . For this specific case,  $f = 4$ ,  $\varphi_c = 0.95$ , and  $\rho = 2, 4, 8$ , and  $16$ . The modulus  $G$  increases with an increase in  $\rho$  since the density of effective strands increases. During elongation, stress fluctuates, reflecting the breakage of some strands. Owing to the energy-minimization scheme, stress immediately goes down to zero when network percolation is eliminated. Conversely, energy dissipation due to network relaxation<sup>26</sup> is not considered. Nevertheless, in addition to the modulus ( $G$ ), strain and stress at break ( $\varepsilon_b$  and  $\sigma_b$ ) and work for fracture ( $W_b$ ) were obtained from each stress-strain curve. (Note that  $W_b$  here is energy per unit volume, and is different from the fracture energy in tearing experiments defined as energy per unit area.) These values were averaged among 8 independent simulations for various  $\rho, f$ , and  $\varphi_c$ , and the data are shown below.

Fig. 4 shows the modulus  $G$  plotted against  $\rho$  for  $\varphi_c = 0.6$  (top) and  $0.95$  (bottom) with various  $f$ . The modulus was obtained as the value of  $\sigma/(\lambda^2 - \lambda^{-1})$  with the stretch  $\lambda$  at  $\lambda^{-1} = 0.75$ , as in the previous study.<sup>11</sup> As mentioned in Fig. 3,  $G$  increases with an increase in  $\rho$ . However,  $G$  is not proportional to  $\rho$  for low  $\rho$ . See the deviation from the dotted lines that indicate the slope of unity. This non-linearity of  $G$  against  $\rho$  reflects that some fractions of network nodes do not effectively sustain stress.

Fig. 5(a) shows  $G$  normalized by the number density of branch points  $v_{\text{br}}$  plotted against cycle rank  $\xi$  for various  $\rho$ .  $v_{\text{br}}$  is defined as  $v_{\text{br}} \equiv M/V = \rho/(fN_a + 1)$  with the volume  $V$ , and unreacted prepolymers and dangling ones are not excluded. The data obtained for various  $f$  and  $\varphi_c$  lie on a master curve depending on  $\rho$ , and  $G/v_{\text{br}}$  decreases with a decrease in  $\rho$ .  $G/v_{\text{br}}$  is not proportional to  $\xi$ , but it indicates weak non-linearity for small  $\xi$ . These discrepancies from the phantom network theory<sup>31</sup> are due to the network maturity; some strands in the

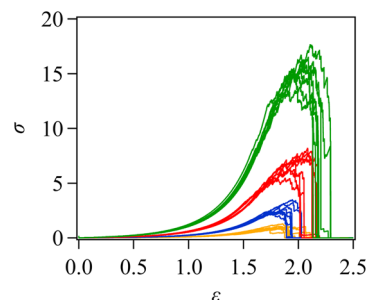


**Fig. 3** True stress versus true strain during elongation for  $f = 4$  and  $\varphi_c = 0.95$ . The results for  $\rho = 2, 4, 8$ , and  $16$  are shown by orange, blue, red, and green curves, respectively. Each curve corresponds to a single simulation run.

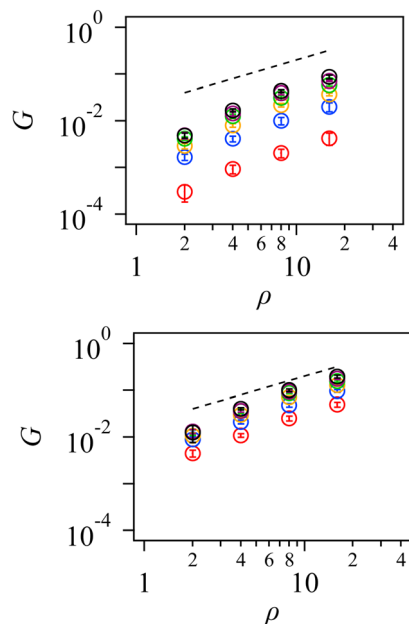


Fig. 4 Modulus  $G$  plotted against  $\rho$  for  $f = 3$  (red), 4 (blue), 5 (orange), 6 (green), 7 (violet), and 8 (black) at  $\phi_c = 0.6$  (top) and 0.95 (bottom). Broken lines indicate the slope of unity. Error bars correspond to the standard deviations for 8 different simulation runs.

percolated network do not contribute to stress. Indeed, Fig. 5(b) shows consistency with the phantom network theory;<sup>31</sup> all the  $G/v_{br}$  data from different  $f$ ,  $\phi_c$ , and  $\rho$  values converge to a single line within the error if they are plotted against the effective cycle rank  $\zeta_{eff}$ , which is obtained from the numbers of nodes and strands actually sustaining stress. As seen in Fig. 5(c),  $\zeta_{eff}$  increases with an increase in  $\rho$ , implying that the network maturity depends on  $\rho$ , and the modulus reflects it.

Fig. 6 shows the fracture characteristics plotted against  $\rho$  for  $\phi_c = 0.6$  (left column) and 0.95 (right column). Concerning  $\varepsilon_b$ , stretch at break  $\lambda_b (= \exp(\varepsilon_b))$  is shown in panels (a1) and (a2). Akagi *et al.*<sup>8</sup> reported for tetra-PEG gels ( $f = 4$ ) with  $\phi_c \sim 0.9$  that  $\lambda_b$  exhibits a power-law dependence on the prepolymer concentration  $\phi$  with the power-law exponent of  $1/3$  ( $\lambda_b \sim \phi^{1/3}$ ). Assuming that  $\phi$  is proportional to  $\rho$ , we add broken lines with a slope of  $1/3$  in panels (a1) and (a2). The simulation results indicated by symbols are inconsistent with this relation. For the case of  $\phi_c = 0.6$  (panel a1),  $\lambda_b$  is almost constant within the examined range of  $\rho$  for  $f > 3$ . For  $f = 3$  (red symbol),  $\lambda_b$  significantly decreases with an increase in  $\rho$ . This behavior is probably due to the difference in  $\phi_c$ ; any experimental reports for networks with such a low conversion ratio cannot be found. However, the discrepancy is also seen for  $\phi_c = 0.95$  (see panel (a2)). A possible reason is explained as follows. In the experiment, polymers are dispersed in a good solvent, and gel networks swell due to osmotic pressure. Such swelling attains the development of a mechanically effective network with relatively homogeneous structures, even under low polymer concentrations. In contrast, our simulations are for phantom chains, and the effect of osmotic force is neglected. Thus, when the prepolymer concentration is low, structural inhomogeneity is

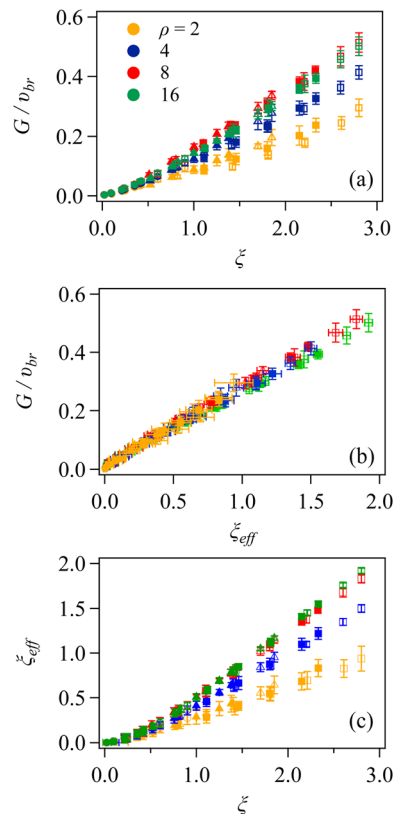
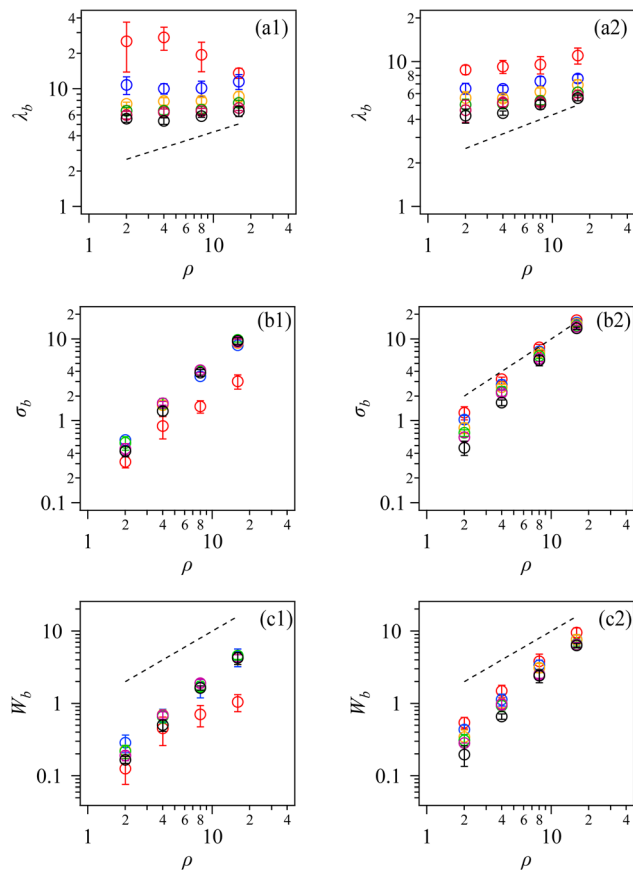


Fig. 5 Modulus  $G$  normalized by the number density of branch points  $v_{br}$  as a function of cycle rank  $\xi$  (a),  $G/v_{br}$  plotted against effective cycle rank  $\zeta_{eff}$  (b) and  $\zeta_{eff}$  versus  $\xi$  (c). Yellow, blue, red, and green symbols indicate the results for the bead density  $\rho$  at 2, 4, 8, and 16, respectively. Symbols indicate  $f = 3$  (filled circle), 4 (unfilled circle), 5 (filled triangle), 6 (unfilled triangle), 7 (filled square), and 8 (unfilled square), respectively. Error bars indicate the standard deviations for 8 different simulation runs.

enhanced as the reaction proceeds, as seen in Fig. 1. The mechanical behaviors reflect this structural difference, at least partly. Note that even for tetra-PEG gels, structural inhomogeneity is observed when the prepolymer concentration is extremely low.<sup>27</sup>

Fig. 6 b and c exhibit  $\sigma_b$  and  $W_b$  plotted against  $\rho$  for various  $f$  values, demonstrating that these fracture characteristics increase with an increase in  $\rho$ . Even though the simulation setting is different from tearing tests, if we assume Lake–Thomas theory and regard  $W_b$  as a quantity comparable to the fracture energy,  $W_b$  is expected to be proportional to  $\rho$ . Broken lines in panels (c1) and (c2) show this behavior, and the simulation results shown by the symbols are qualitatively consistent. However, some discrepancies are also observed. For instance, the  $\rho$ -dependence of  $W_b$  is somewhat more intense than the broken line when  $\rho$  is low and  $f$  is large.  $W_b$  for the case with  $f = 3$  and  $\phi_c = 0.6$  (red circle in panel c1) saturates in the high  $\rho$  regime. Note, however, that the fracture energy in tearing tests is defined as the energy per unit area, whereas  $W_b$  here is the energy per unit volume; thus, straightforward comparison is difficult.

One might argue that the results depicted in Fig. 6 reflect not just the effect of density but also of the system size, given



**Fig. 6** Stretch at break  $\lambda_b \equiv \exp(\varepsilon_b)$  (panels a), stress at break  $\sigma_b$  (panels b), and work for fracture  $W_b$  (panels c) plotted against the bead number density  $\rho$  at  $\varphi_c = 0.6$  (left column) and  $0.95$  (right column) for  $f = 3$  (red), 4 (blue), 5 (orange), 6 (green), 7 (violet), and 8 (black). Error bars correspond to the standard deviations for 8 different simulation runs. Broken curves in panels a and c indicate slopes of  $1/3$  and unity.

that the simulation box dimensions varied, as shown in Fig. 1. For this matter, we present results with a fixed box dimension, filled with varying numbers of molecules. Fig. 7 illustrates  $\varepsilon_b$ ,  $\sigma_b$ , and  $W_b$  for  $f = 4$  at  $\varphi_c = 0.6$  and  $0.95$ , across various  $\rho$ , with a constant box volume. The results align with those in Fig. 6, where the number of molecules was fixed, thereby indicating that the effect of the system size is insignificant.

Fig. 8 exhibits all the obtained fracture characteristic values for various sets of  $\rho$ ,  $f$ , and  $\varphi_c$  plotted against  $\xi$ . For each  $\rho$ ,  $\varepsilon_b$  data in panel (a) are located on a master curve described as a power-law decay function of  $\xi$ ;  $\varepsilon_b = A_\varepsilon \xi^{-\alpha_\varepsilon}$ . The power-law dependence can be confirmed in the double logarithmic plot exhibited in the right panel. As  $\rho$  increases,  $\varepsilon_b$  slightly increases systematically. As reported previously,<sup>11–13</sup>  $\sigma_b$  and  $W_b$  for various  $f$  and  $\varphi_c$  also lie on master curves if these values divided by  $v_{br}$  are plotted against  $\xi$ . In a similar manner to  $\varepsilon_b$ , these behaviors are described by power-law functions of  $\xi$ ;  $\sigma_b/v_{br} = A_{\sigma_b} \xi^{\alpha_\sigma}$  and  $W_b/v_{br} = A_{W_b} \xi^{\alpha_{W_b}}$ . As  $\rho$  increases, both  $\sigma_b/v_{br}$  and  $W_b/v_{br}$  increase. The master curves have been previously reported for  $\rho = 8$ , but they are found for the first time for the other  $\rho$  values. Note that in the previous study,<sup>11</sup>  $\sigma_b$  and  $W_b$  were normalized by

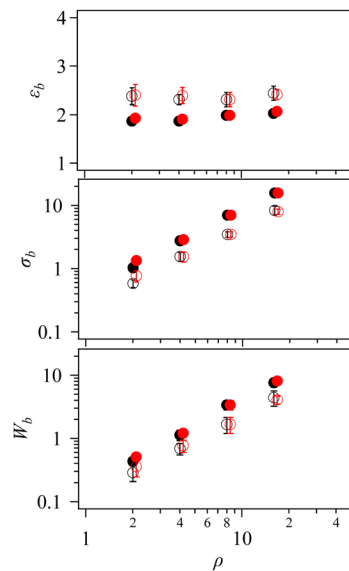


**Fig. 7** Strain at break  $\varepsilon_b$ , stress at break  $\sigma_b$ , and work for fracture  $W_b$  from top to bottom plotted against the bead number density  $\rho$  for  $f = 4$  at  $\varphi_c = 0.6$  (unfilled circle) and  $0.95$  (filled circle) for the simulation with a constant volume (red) and with a constant prepolymer number (black). For the constant volume simulation, the volume  $V$  was fixed at 4200, and the number of prepolymers  $M$  was varied as 400, 800, 1600, and 3200. For the simulation with a constant prepolymer number,  $M = 1600$  and  $V = 16800$ , 8400, 4200, and 2100. Error bars correspond to the standard deviations for 8 different simulation runs and are sometimes smaller than the symbols. To avoid overlaps, red and black symbols are shown with horizontal offsets.

the broken strand fraction  $\varphi_{bb}$ . However, the  $\varphi_{bb}$  value is hardly experimentally accessible, and  $v_{br}$  was found to achieve the master curves instead of  $\varphi_{bb}$  in another previous study.<sup>13</sup>

Fig. 9 exhibits the parameters for the power-law functions plotted against  $\rho$ . Reflecting the weak  $\rho$ -dependence of  $\varepsilon_b$  in Fig. 8, the power-law exponent  $\alpha_\varepsilon$  and the factor  $A_\varepsilon$  vary against  $\rho$  only slightly. The exponents for  $\sigma_b/v_{br}$  and  $W_b/v_{br}$  are similar and increase with an increase in  $\rho$ , as seen in Fig. 8. The change against  $\rho$  is similar also for the factors.

We emphasize that the power-law fittings in Fig. 8 are just for eye guidance. Since no theoretical explanation has been found at present, better functional forms may exist to fit the data. Specifically, the fracture characteristics must be lower-limited due to a minimum stretch below which fracture does not occur. The power-law expressions are not compatible with such an intuition.

One may argue that Fig. 5 and 8 suggest a correlation between the modulus and the fracture characteristics. Fig. 10 examines such an argument. For each  $\rho$  case,  $\sigma_b/v_{br}$  and  $W_b/v_{br}$  are single-valued functions of  $G/v_{br}$ . Namely, the fracture behavior for the networks with various  $f$  and  $\varphi_c$  values is dominated by the modulus, given that  $\rho$  is common. However, when  $\rho$  differs, networks sharing the same  $G/v_{br}$  value exhibit different  $\sigma_b/v_{br}$  and  $W_b/v_{br}$  values; these values increase with an increase in  $\rho$ . Consequently, the fracture characteristics are not solely described by the modulus. These results are consistent with the experiment by Fujiyabu *et al.*,<sup>9</sup> who demonstrated that

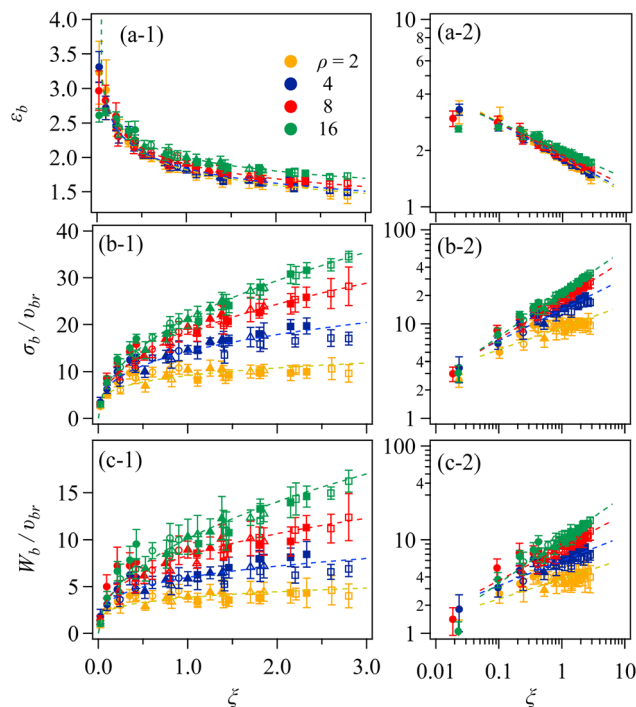


**Fig. 8** Fracture characteristics  $\varepsilon_b$ ,  $\sigma_b$ , and  $W_b$  obtained for various  $\rho$ ,  $f$ , and  $\varphi_c$  values as functions of  $\xi$ .  $\sigma_b$  and  $W_b$  are normalized by the branch point density  $v_{br}$ . The right panels show logarithmic plots. The  $f$  values are 3 (filled circle), 4 (unfilled circle), 5 (filled triangle), 6 (unfilled triangle), 7 (filled square), and 8 (unfilled square), respectively. Error bars are standard deviations among eight different simulation runs. Broken curves show power-law functions;  $\varepsilon_b = A_\varepsilon \xi^{-\alpha_\varepsilon}$ ,  $\sigma_b/v_{br} = A_\sigma \xi^{\alpha_\sigma}$  and  $W_b/v_{br} = A_W \xi^{\alpha_W}$ .

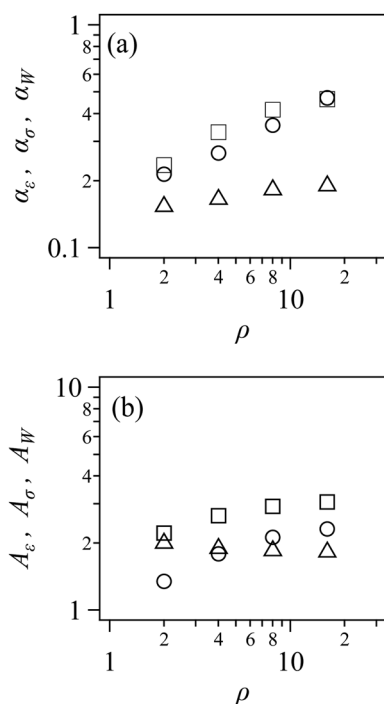


**Fig. 9** Parameters employed for the power-law fittings in Fig. 8; the power-law exponents (a) and the factors (b) plotted against  $\rho$ . Triangle, square, and circle show the parameters for  $\varepsilon_b$ ,  $\sigma_b$ , and  $W_b$ , respectively.

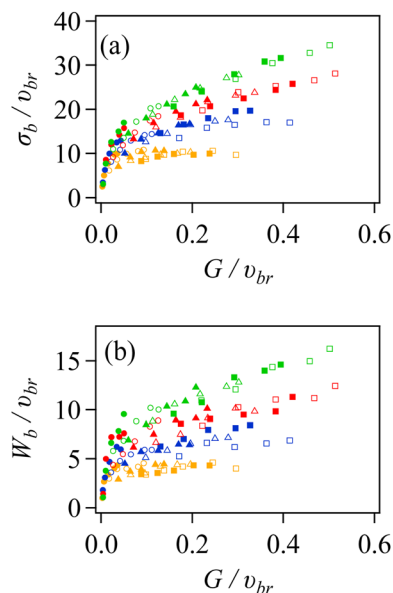


**Fig. 10** Fracture characteristics  $\sigma_b/v_{br}$  (a) and  $W_b/v_{br}$  (b) obtained for various  $\rho$ ,  $f$ , and  $\varphi_c$  values plotted against  $G/v_{br}$ . The  $f$  values are 3 (filled circle), 4 (unfilled circle), 5 (filled triangle), 6 (unfilled triangle), 7 (filled square), and 8 (unfilled square), respectively. The  $\rho$  values are 2 (yellow), 4 (blue), 8 (red), and 16 (green), respectively.

tetra-PEG and tri-PEG gels exhibit different fracture characteristics even if the modulus is tuned to be common. Note that the results in Fig. 5 and 10 also imply that the curves in Fig. 8 do not converge to a single curve even if the values are plotted against  $\xi_{eff}$ ; according to Fig. 5(b), a plot against  $G/v_{br}$  is essentially the same as that against  $\xi_{eff}$ .

The results shown in Fig. 10 imply that network maturity evaluated by the modulus differs from that affects fracture properties. Modulus is used to quantify the density of effective strands and nodes, and their mechanical contributions appear as an averaged value. In contrast, the fracture is initiated by the scission of the most elongated strand and propagates to the next ones in a cascade manner. Since we conducted simulations with step-by-step energy minimization, this propagation occurs within the elongated tail of the strand length distribution. Therefore, modulus and fracture reflect different characteristics of the strand length statistics that are unnecessarily correlated.

## Conclusions

We conducted phantom chain simulations to investigate the effect of prepolymer concentration on the fracture behavior of star polymer networks. We varied the star polymer functionality  $f$  from 3 to 8, the conversion ratio  $\varphi_c$  from 0.6 to 0.95, and the segment number density  $\rho$  from 2 to 16. The resultant networks were statistically evaluated regarding the cycle rank  $\xi$ , consistent with the mean-field theory, demonstrating that the end-linking reactions occurred independently. We uniaxially stretched the networks and obtained modulus  $G$  and fracture characteristics, including strain at break  $\varepsilon_b$ , stress at break  $\sigma_b$ ,

and work for fracture  $W_b$  from the stress–strain relationship until the break. Consistent with experiments, these mechanical characteristics increase with an increase in  $\rho$ . With the branch point density  $\nu_{br}$ , if we plot  $G/\nu_{br}$ ,  $\epsilon_b$ ,  $\sigma_b/\nu_{br}$ , and  $W_b/\nu_{br}$  against  $\xi$ , the data for various  $f$  and  $\varphi_c$  are located on master curves, as reported previously. However, different curves are realized for different  $\rho$  values. We also found that if we plot  $\sigma_b/\nu_{br}$  and  $W_b/\nu_{br}$  against  $G/\nu_{br}$ , master curves are seen for various  $f$  and  $\varphi_c$ , but they depend on  $\rho$ . This result demonstrates that fracture is not solely dominated by the modulus but also depends on the prepolymer density.

Although the presented study gives fundamental information about network fracture, it is fair to note that the reported  $\xi$ -dependence of fracture characteristics has not been experimentally confirmed. The reason is that few datasets report fractures of networks with a sufficient range of  $f$  and  $\varphi_c$  values. In particular,  $\varphi_c$  needs to be clarified in most literature reports. We should also note that the results may change if we consider osmotic force, excluded volume interactions, and thermal fluctuations. Besides, we have not found any interpretation of the significance of cycle rank, which may be better converted to other structural parameters that include the opening loop length<sup>6</sup> and the minimum path length.<sup>32</sup> Subsequent studies such directions are ongoing, and the results will be reported elsewhere.

## Data availability

The simulation code is available at [https://osf.io/fxnbe/?view\\_only=e0af4fa18a524397a309adc9f0089bcbf](https://osf.io/fxnbe/?view_only=e0af4fa18a524397a309adc9f0089bcbf).

## Conflicts of interest

There are no conflicts to declare.

## Acknowledgements

This study was partly supported by JST-CREST (JPMJCR1992) and JSPS KAKENHI (22H01189).

## References

- 1 T. Sakai, *Physics of Polymer Gels*, Wiley, 2020.
- 2 C. W. Barney, Z. Ye, I. Sacligil, K. R. McLeod, H. Zhang, G. N. Tew, R. A. Riggleman and A. J. Crosby, *Proc. Natl. Acad. Sci. U. S. A.*, 2022, **119**, 2–7.
- 3 M. Zhong, R. Wang, K. Kawamoto, B. D. Olsen and J. A. Johnson, *Science*, 2016, **353**, 1264–1268.
- 4 J. Lake and A. G. Thomas, *Proc. R. Soc. London, Ser. A*, 1967, **300**, 108–119.
- 5 S. Lin and X. Zhao, *Phys. Rev. E*, 2020, **102**, 52503.
- 6 S. Wang, C. M. Hartquist, B. Deng and X. Zhao, *Macromolecules*, 2024, **57**, 6069–6075.
- 7 S. Wang, S. Panyukov, S. L. Craig and M. Rubinstein, *Macromolecules*, 2023, **56**, 2309–2318.
- 8 Y. Akagi, T. Katashima, H. Sakurai, U. Il Chung and T. Sakai, *RSC Adv.*, 2013, **3**, 13251–13258.
- 9 T. Fujiyabu, N. Sakumichi, T. Katashima, C. Liu, K. Mayumi, U. Chung and T. Sakai, *Sci. Adv.*, 2022, **8**, abk0010\_1–abk0010\_10.
- 10 Y. Masubuchi, Y. Doi, T. Ishida, N. Sakumichi, T. Sakai, K. Mayumi and T. Uneyama, *Macromolecules*, 2023, **56**, 2217–2223.
- 11 Y. Masubuchi, Y. Doi, T. Ishida, N. Sakumichi, T. Sakai, K. Mayumi, K. Satoh and T. Uneyama, *Macromolecules*, 2023, **56**, 9359–9367.
- 12 Y. Masubuchi, *Polym. J.*, 2024, **56**, 163–171.
- 13 Y. Masubuchi, *Polymer*, 2024, **297**, 126880.
- 14 T. Sakai, *Nihon Reoroji Gakkaishi*, 2019, **47**, 183–195.
- 15 M. Shibayama, X. Li and T. Sakai, *Colloid Polym. Sci.*, 2019, **297**, 1–12.
- 16 T. Sakai, Y. Akagi, S. Kondo and U. Chung, *Soft Matter*, 2014, **10**, 6658–6665.
- 17 Y. Masubuchi, *Nihon Reoroji Gakkaishi*, 2024, **52**, 21–26.
- 18 R. L. Honeycutt, *Phys. Rev. A: At., Mol., Opt. Phys.*, 1992, **45**, 600–603.
- 19 Y. Masubuchi, R. Yamazaki, Y. Doi, T. Uneyama, N. Sakumichi and T. Sakai, *Soft Matter*, 2022, **18**, 4715–4724.
- 20 Y. Masubuchi and T. Uneyama, *Soft Matter*, 2019, **15**, 5109–5115.
- 21 M. Lang, *Macromolecules*, 2019, **52**, 6266–6273.
- 22 K. Nishi, H. Noguchi, T. Sakai and M. Shibayama, *J. Chem. Phys.*, 2015, **143**, 184905.
- 23 K. Nishi, M. Chijiishi, Y. Katsumoto, T. Nakao, K. Fujii, U. Chung, H. Noguchi, T. Sakai and M. Shibayama, *J. Chem. Phys.*, 2012, **137**, 224903.
- 24 J. Lei, Z. Li, S. Xu and Z. Liu, *J. Mech. Phys. Solids*, 2021, **156**, 104599.
- 25 J. Nocedal, *Math. Comput.*, 1980, **35**, 773.
- 26 A. Arora, T. S. Lin and B. D. Olsen, *Macromolecules*, 2022, **55**, 4–14.
- 27 S. Ishikawa, Y. Iwanaga, T. Uneyama, X. Li, H. Hojo, I. Fujinaga, T. Katashima, T. Saito, Y. Okada, U. Chung, N. Sakumichi and T. Sakai, *Nat. Mater.*, 2023, **22**, 1564–1570.
- 28 C. W. Macosko and D. R. Miller, *Macromolecules*, 1976, **9**, 199–206.
- 29 C. W. Macosko and D. R. Miller, *Makromol. Chem.*, 1991, **192**, 377–404.
- 30 Y. Yoshikawa, N. Sakumichi, U. Chung and T. Sakai, *Soft Matter*, 2019, **15**, 5017–5025.
- 31 H. M. James and E. Guth, *J. Chem. Phys.*, 1943, **11**, 455–481.
- 32 Z. Yu and N. E. Jackson, *arXiv*, 2024, preprint, arXiv:2405.03551, DOI: [10.48550/arXiv.2405.03551](https://doi.org/10.48550/arXiv.2405.03551).